

# Long term time dependent frequency analysis of chaotic waves in the weakly magnetised spherical Couette system

Ferran Garcia, Martin Seilmayer, André Giesecke, Frank Stefani

*Helmholtz-Zentrum Dresden-Rossendorf, Bautzner Landstraße 400, D-01328 Dresden, Germany*

---

## Abstract

The long term behaviour of chaotic flows obtained when an electrically conducting fluid, confined between two differentially rotating spheres, is subjected to an axial magnetic field is investigated by means of time dependent frequency analysis. The classical Fourier Transform method provides a first estimation of the time dependence of the frequencies associated to the flow, as well as its volume-averaged properties, but it is unable to detect strange attractors close to regular solutions in the Feigenbaum as well as Newhouse-Ruelle-Takens bifurcation scenarios. It is shown that Laskar's frequency algorithm is sufficiently accurate to identify these strange attractors and thus is an efficient tool for a rigorous classification of chaotic flows in high dimensional dynamical systems. Our analysis of several chaotic solutions, obtained at different magnetic field strengths, reveals a strong robustness of the main frequency of the flow. This frequency is associated to an azimuthal drift and it is very close to the frequency of the underlying unstable rotating wave. In contrast, the main frequency of volume-averaged properties can vary almost one order of magnitude as the magnetic forcing is decreased.

We conclude that, at the moderate differential rotation considered, unstable rotating waves provide a good description of the variation of the main time scale of any flow with respective variations in the magnetic field.

*Keywords:* Frequency Analysis, Chaos, Magnetohydrodynamics

---

## 1. Introduction

The magnetized spherical Couette (MSC) system -a liquid metal within two differentially rotating spheres subject to a magnetic field- represents one of the fundamental problems for studying three-dimensional magnetohydrodynamic (MHD) instabilities [1, 2, 3, 4, 5]. The coupled effects of rotation, magnetic fields and spherical geometry, are indeed common in a wide range of processes occurring in celestial objects [6, 7], including the generation of the Sun's [8] and the Earth's magnetic fields [9], or the transport mechanisms in accretion disks around black holes, stars, and protoplanetary disks [10]. The latter have been interpreted in terms of the magnetorotational instability (MRI) [11] which is nowadays considered the best explanation.

Starting with [11] the occurrence of the MRI has been studied in great detail including numerical and experimental work. Experimental investigations of the MRI were conducted at the Helmholtz-Zentrum Dresden-Rossendorf (HZDR) using the GaInSn liquid metal alloy within two rotating cylinders [12, 13, 14], and in Maryland [15] with liquid sodium in spherical geometry. The latter experiment [15] motivated recent numerical studies [2, 3] which, however, provided alternative interpretations of the observed instabilities in terms of typical instabilities in magnetised spherical Couette (MSC) flows.

To shed light onto this controversy, the HEDGEHOG experiment (Hydro-magnetic Experiment with Differentially Gyating sphEres HOlding GaInSn) has been designed, at the HZDR, to describe three-dimensional magnetohydrodynamic instabilities, which are related to the hydrodynamic jet instability, the return flow instability and the Kelvin-Helmholtz-like Shercliff layer instability (see [16] and the references therein). These instabilities have been studied in the past [2, 3, 17, 4] by means of direct numerical simulations DNS of the MSC system, and their spatio-temporal symmetries and nonlinear dynamics have been recently described in terms of bifurcation and dynamical systems theory [5, 18, 19]. We refer to the introductory sections of these latter studies for a detailed summary and references on the numerical studies in the field.

The MSC system is  $\mathbf{SO}(2) \times \mathbf{Z}_2$ -equivariant, i. e., invariant by azimuthal rotations and reflections with respect to the equatorial plane, and thus a rich variety of nonlinear dynamics is expected [20] thanks to flow bifurcations occurring as the parameters  $\text{Re}$  (the Reynolds number measuring rotation rates) and  $\text{Ha}$  (the Hartmann number measuring magnetic field strength) are varied. The typical sequence of bifurcations (Hopf, period-doubling) in these systems [20, 21, 22, 23] has been described recently at moderate  $\text{Re} = 10^3$  and  $\text{Ha} < 80$ , addressing the numerical continuation of rotating waves [5], the theoretical description of modulated rotating waves [18], and the appearance of complex waves and chaotic flows [19]. The present study extends this previous work by analysing the long term behaviour of the flows, with special focus on the estimation of the main time scales involved in chaotic flows. The numerical approach relies on a time dependent

frequency spectrum analysis of very long time series, including global as well as local flow properties. Laskar's algorithm [24, 25, 26], implemented in the SDDS Toolkit [27], provides a useful tool for an accurate determination of the fundamental frequencies of a time series. Moreover, the study of the time dependent spectrum provides an estimation of the diffusion of the orbit in the phase space [28] and thus can be used to identify chaotic flow behaviour and to study global dynamics. There exist other even more accurate algorithms for the determination of fundamental frequencies, for instance those based on collocation methods developed in [29, 30] and the references therein, which have been used successfully as dynamical indicators. The idea of the analysis of the time-frequency dependence is common (see for instance [31] or the very recent comparison [32]) to assess the chaotic behaviour of a nonlinear system.

We recall that for a more complete description of chaos the computation of the so called Lyapunov characteristic exponents (LCE) [33, 34, 35] must be performed and that for this purpose time series tools are available [36]. The latter, are based on phase space reconstruction using the method of delays [37] and require the adjustment of several parameters such as the embedding dimension or the time delay. In comparison with those techniques, Laskar's analysis can be applied in a more straightforward manner and only requires to control the accuracy of the obtained frequencies. A comprehensive analysis of methods for computing LCE, including those based on direct time integrations of the evolution equations and those based on time series, has been recently performed in [38] for simple systems. In addition, the latter study [38] provides a description of the dynamics in terms of Fourier spectra

and Gauss wavelets. The comparison was extended to a system with  $O(10^2)$  degrees of freedom in [39] illustrating main problems and difficulties of LCE estimation from a time series.

With the present study we demonstrate the applicability of Laskar's algorithm, a highly accurate tool for the determination of fundamental frequencies, for identifying chaotic motions in a dissipative dynamical system, with a large number  $\sim O(10^5)$  of degrees of freedom, due to the spatial discretisation of partial differential equations. This is demonstrated for first time in the context of MHD, at least in spherical geometry. In addition, the study is based on very large time evolutions (more than order of magnitude larger than the previous studies in the MSC context) which is a challenging task given the dimension of the problem. With the analysis of the time dependent spectrum, for two different routes to chaos, the main result found is a strong robustness of the temporal scale associated to an azimuthal flow drift, even for highly oscillatory chaotic flows.

The structure of the paper is the following: In § 2 the problem and the numerical method used to integrate the model equations are formulated, and the data used for the spectral analysis is described. In § 3 a study of the accuracy for the frequency determination and the set-up for the time dependent spectra, is provided. The results are discussed in § 4, considering the Newhouse-Ruelle-Takens [40] as well as Feigenbaum routes to chaos, and finally in § 5 the paper closes with a discussion on the main results obtained.

## 2. The model and methods

In the HEDGEHOG experiment a liquid metal (GaInSn) fills the gap between two spheres of radius  $r_i$  and  $r_o$  with  $\chi = r_i/r_o = 0.5$ . The inner sphere is rotating with constant velocity  $\Omega$  around the vertical axis  $\hat{\mathbf{e}}_z$  while the outer is at rest. In addition, an axial magnetic field of amplitude  $B_0$  is applied to the system, see Fig. 1, and insulating boundary conditions are considered for the magnetic field outside the fluid region [1].

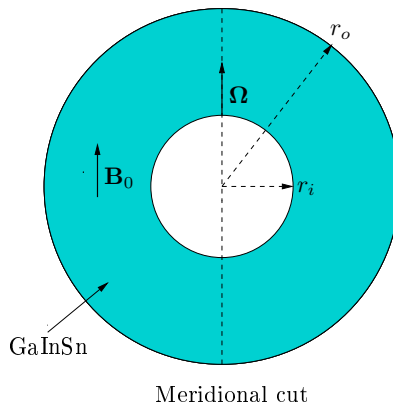


Figure 1: Geometrical configuration of the magnetized spherical Couette (MSC) problem.

### 2.1. The governing equations

The mathematical formulation of the problem [1] relies on the inductionless approximation of the Navier-Stokes and induction equations. This approximation remains valid when the magnetic Reynolds number  $\text{Rm} = \Omega r_i d / \eta$ ,  $\eta$  being the magnetic diffusivity and  $d = r_o - r_i$ , is small  $\text{Rm} \ll 1$ . In case of the HEDGEHOG experiment the GaInSn eutectic alloy [41] has very low magnetic Prandtl number  $\text{Pm} = \nu / \eta \sim O(10^{-6})$ ,  $\nu$  being the

kinematic viscosity, and the values for the Reynolds numbers are moderate  $\text{Re} = \Omega r_i d / \nu \sim 10^3$ . This means that  $\text{Rm} = \text{PmRe} \sim 10^{-3}$  and thus the inductionless constraint is fulfilled.

The equations of motion are

$$\partial_t \mathbf{v} + \text{Re}(\mathbf{v} \cdot \nabla) \mathbf{v} = -\nabla p + \nabla^2 \mathbf{v} + \text{Ha}^2 (\nabla \times \mathbf{b}) \times \hat{\mathbf{e}}_z, \quad (1)$$

$$0 = \nabla \times (\mathbf{v} \times \hat{\mathbf{e}}_z) + \nabla^2 \mathbf{b}, \quad (2)$$

$$\nabla \cdot \mathbf{v} = 0, \quad \nabla \cdot \mathbf{b} = 0. \quad (3)$$

where  $p$  is the dimensionless pressure containing all the potential forces,  $\mathbf{v}$  is the velocity field and  $\mathbf{b}$  is the magnetic field perturbation of the axially applied field  $\mathbf{B} = \hat{\mathbf{e}}_z + \text{Rm}\mathbf{b}$ . For the velocity field the no-slip ( $v_r = v_\theta = v_\varphi = 0$ ), at  $r = r_o$ , and constant rotation ( $v_r = v_\theta = 0$ ,  $v_\varphi = \sin \theta$ ), at  $r = r_i$ , conditions are imposed on the boundaries. For the magnetic field, the exterior regions are assumed to be insulating as it is the case for the HEDGEHOG experiment.

The system is governed by 3 non-dimensional numbers:

$$\text{Re} = \frac{\Omega r_i d}{\nu}, \quad \text{Ha} = \frac{B_0 d}{\sqrt{\rho \nu \mu_0 \eta}}, \quad \chi = \frac{r_i}{r_o},$$

$\mu_0$  being the free-space value for the magnetic permeability, and  $\rho$  being the density of the fluid. The parameters selected for the present study,  $\chi = 0.5$ ,  $\text{Re} = 10^3$  and  $\text{Ha} < 6$ , are in accordance with the typical operating parameters of the HEDGEHOG experiments which are  $\eta = 0.35, 0.5$ ,  $\text{Re} \in [10^3, 10^4]$  and  $\text{Ha} < 10^3$ .

## 2.2. Numerical Approach

The pseudo-spectral method for the numerical solution of the governing equations is briefly described in the following. For full details we refer to [5]

and references therein.

The divergence-free velocity field is expressed as a sum of the toroidal,  $\Psi$ , and poloidal,  $\Phi$ , potentials

$$\mathbf{v} = \nabla \times (\Psi \mathbf{r}) + \nabla \times \nabla \times (\Phi \mathbf{r}), \quad (4)$$

and the unknowns are expanded in spherical harmonics series in the angular coordinates,  $\mathbf{r} = r \hat{\mathbf{e}}_r$  being the position vector. For the radial coordinate a collocation method on a Gauss-Lobatto mesh of  $N_r$  points is employed. Specifically, the scalar potentials (Eq. 4) are expanded in spherical harmonic series up to degree  $L_{\max}$  and order  $M_{\max} = L_{\max}$  as

$$\Psi(t, r, \theta, \varphi) = \sum_{l=0}^{L_{\max}} \sum_{m=-l}^l \Psi_l^m(r, t) Y_l^m(\theta, \varphi), \quad (5)$$

$$\Phi(t, r, \theta, \varphi) = \sum_{l=0}^{L_{\max}} \sum_{m=-l}^l \Phi_l^m(r, t) Y_l^m(\theta, \varphi), \quad (6)$$

with  $\Psi_l^{-m} = \overline{\Psi_l^m}$  and  $\Phi_l^{-m} = \overline{\Phi_l^m}$ . By choosing  $\Psi_0^0 = \Phi_0^0 = 0$  the two scalar potentials are uniquely determined. We recall that  $Y_l^m(\theta, \varphi) = P_l^m(\cos \theta) e^{im\varphi}$  is the spherical harmonic function,  $P_l^m$  being the normalised associated Legendre functions of degree  $l$  and order  $m$ . The computation of the nonlinear (advection) term relies on the use of fast optimised libraries (FFTW3 [42]) for the FFTs in longitude, and matrix-matrix products (dgemm GOTO [43]) for the Legendre transforms in latitude. The code is parallelised on the spectral and on the physical space by using OpenMP directives.

After the discretization of Eqs. (1-3) a system of ordinary differential equations (ODE) of dimension  $n = (2L_{\max}^2 + 4L_{\max})(N_r - 1)$  is obtained:

$$L_0 \partial_t u = Lu + B(u, u), \quad (7)$$

with  $u$  the vector of spherical harmonic amplitudes of the velocity potentials at the radial mesh (without considering the boundaries).  $L_0$  and  $L$  are linear operators including the boundary conditions,  $L_0$  being invertible. The operator  $L$  is linear and depends on the Hartmann number  $Ha$ . The bilinear operator  $B$  contains the non-linear (quadratic) terms.

High order implicit-explicit backward differentiation formulas (IMEX–BDF) [44] are used for the time integration of Eq. 7. The nonlinear terms are considered explicitly to avoid the solution of a nonlinear system at each time step. An explicit treatment of the Lorenz force term facilitates the implementation of the linear solver, but may lead to smaller time integration steps ( $\Delta t$ ) in comparison with an implicit treatment. However, this is not critical as moderate  $Ha$  are considered in the present study.

### 2.3. Output data and azimuthal symmetry

Two different diagnostics are considered in the present study. First, the time series of the radial velocity  $v_r$  picked up at the point  $(r, \theta, \varphi) = (r_i + 0.5d, \pi/8, 0)$ , which is a local measurable that reflects the time scales of the flow. Second, the time series of the volume-averaged kinetic energy  $K$ , defined as

$$K = \frac{1}{2\mathcal{V}} \int_{\mathcal{V}} \mathbf{v} \cdot \mathbf{v} \, dv, \quad (8)$$

provides a global measure. Instead of considering  $K$  for the total flow, we compute the kinetic energy  $K_m$  defined by only employing the spherical harmonic amplitudes  $\Psi_l^m$  and  $\Phi_l^m$  with order  $m$  and degree  $|m| \leq l \leq L_{\max}$ . This provides an idea on the distribution of kinetic energy among the different azimuthal modes  $m$ . For the flows we are analysing (see [19]) there

exists an  $m_{\max}$  with  $\overline{K}_{m_{\max}} \gg \overline{K}_m$ ,  $1 \leq m \leq L_{\max}$ ,  $m \neq m_{\max}$ ,  $\overline{K}$  being the time average. We note then that the flow will exhibit  $m_{\max}$  vortices. If in addition the flow has  $m_d$ -fold azimuthal symmetry, then it is unaffected by azimuthal rotations multiple of  $2\pi/m_d$  and the spherical harmonic amplitudes with azimuthal wave numbers being multiples of  $m_d$  are the only nonzero in Eqs. (5-6). Notice that if the azimuthal symmetry is  $m_d = 1$  all the spherical harmonics amplitudes are considered.

### 3. Frequency analysis

For an accurate determination of the fundamental frequencies of a time series, Laskar's method [26] of numerical analysis of fundamental frequencies (NAFF) is employed. This method, implemented in the SDDSToolKit, involves a Hanning window and FFT together with a numerical optimisation of the difference between the signal and exponential functions of time.

#### 3.1. Accuracy estimation

In order to estimate the accuracy of Laskar's algorithm for the determination of the frequency with the largest amplitude, a rotating wave (also travelling) wave (RW) with azimuthal symmetry  $m = 4$  and rotating frequency  $\omega$  is considered (i. e. a periodic flow which temporal dependence can be described as  $u(t, r, \theta, \varphi) \equiv u(r, \theta, \varphi - \omega t)$ ). The parameters of this RW are  $\chi = 0.5$ ,  $\text{Re} = 10^3$  and  $\text{Ha} = 3.7766571$ .

Because a RW is a periodic orbit, it can be obtained by means of a continuation method [5] and its rotating frequency estimated up to a prescribed tolerance. Specifically, we solve a nonlinear system which determines a single

RW defined by  $x = (u, \tau, p)$ ,  $\tau = 2\pi/(m\omega)$  being the period, at a parameter  $p = \text{Ha}$ . The system is

$$H(u, \tau, p) = \begin{pmatrix} u - \phi(\tau, u, p) \\ g(u) \\ m(u, \tau, p) \end{pmatrix} = 0, \quad (9)$$

where  $\phi(\tau, u, p)$  is a solution of Eq. (7) at time  $\tau$  and initial condition  $u$  for fixed  $p$ . The condition  $g(u) = 0$  is selected to fix the undetermined phase of the RW and  $m(u, \tau, p)$  is the pseudo-arclength condition of the continuation method. This system is solved by employing a Newton-Krylov procedure with tolerance  $10^{-8}$ . Newton-Krylov are matrix-free methods which do not require the explicit computation of the Jacobian  $D_{(u,\tau,p)}H(u, \tau, p)$ , but only its action on a given vector (see [5] for full details).

Once the RW with  $m = 4$  at  $\text{Ha} = 3.7766571$  has been obtained with the Newton-Krylov procedure, a direct time integration of the MSC equations is performed to obtain the time series of the radial velocity  $v_r$  picked up at the point  $(r, \theta, \varphi) = (r_i + 0.5d, \pi/8, 0)$  for which Laskar's algorithm is applied subsequently. The step for the time integration is the same,  $\Delta t = 5 \times 10^{-6}$ , as that used for the time integration within Newton's method. We note that this  $\Delta t$  provides enough accuracy (we have used a 4th order time scheme) with errors less than  $10^{-8}$  because otherwise Newton's method does not converge. The use of high order time integration methods [44] is recommended when a highly accurate time integration is required.

Newton's method (with tolerance  $10^{-8}$ ) gives  $\omega = 138.09097$  which corresponds to  $f = m\omega/2\pi = 87.91144$  whereas Laskar's algorithm result is  $f = 87.91145$  for  $T \geq 0.3$ ,  $T$  being the time interval of the time series from

which the frequency  $f$  has been computed. The sampling time interval is  $\Delta t_{\text{samp}} = 10^{-4}$  dimensionless time units. For  $T = 0.1$   $f = 87.91068$  and for  $T = 0.2$   $f = 87.91151$ . By decreasing  $\Delta t_{\text{samp}} = 10^{-5}$  the same results are obtained, but for  $\Delta t_{\text{samp}} = 2 \times 10^{-4}$  the accuracy is degraded to  $f = 87.91167$  even for  $T = 20$ .

### 3.2. Time dependent frequency spectrum

Our analysis is based on very long time integrations spanning around  $T_f = 100$  dimensionless time units, which corresponds to  $2 \times 10^7$  time integration steps ( $\Delta t = 5 \times 10^{-6}$ ). This is a challenging task because of the large dimension  $n \sim O(10^5)$  of the ODE system due to the spatial discretisation of the MSC governing equations. By considering the kinematic viscosity of the eutectic alloy GaInSn approximated by  $\nu = 3.4 \times 10^{-3} \text{cm}^2 \text{s}^{-1}$  (see Ref. [41]) the time scale in seconds is  $t^* = td^2/\nu = 5.96 \times 10^3 t$ ,  $t$  being the dimensionless time and the gap width  $d = r_o r_i = 9 \text{ cm} 4.5 \text{ cm} = 4.5 \text{ cm}$ . Thus  $T_f = 100$  represents around 7 days of the HEDGEHOG experiment, which largely exceeds the typical range of the experimental runs (up to 8 hours).

Given a flow initial condition  $u \in \mathbb{R}^n$ , which will be detailed in the next section, the frequency  $f$  of maximum amplitude is computed from a time window  $[t, t + T] \subset [0, T_f]$  of the time series. According to [28] this provides the map

$$\begin{aligned} F_T : \mathbb{R}^n \times \mathbb{R} &\longrightarrow \mathbb{R} \\ (u, t) &\longrightarrow f(u, t) \end{aligned}$$

which can be used for the analysis of the diffusion of the orbit  $u \in \mathbb{R}^n$  with

respect to time, and thus infer the regular or chaotic behaviour of the orbit. If the flow is quasiperiodic  $F_T$  is a constant function of time whereas for chaotic flows  $F_T$  varies indicating the diffusion of the orbit in phase space.

As noticed in [28] the frequencies are computed up to a certain accuracy,  $\epsilon_f$ , depending on the solution  $u$  and the time window  $T$ . For the case of a rotating wave, we have shown in the previous section that this accuracy is about  $\epsilon_f = 10^{-5}$  even for very small time windows  $T = 0.3$ . For the analysis of quasiperiodic and chaotic flows we assume slightly larger discrepancies  $\epsilon_f$ . Then, flows are considered regular if  $F_T$  is constant within  $\epsilon_f$  of accuracy, otherwise are chaotic. Following [28] we also estimate the instantaneous diffusion rate as  $\delta F_T(u, t) = |F_T(u, t + T) - F_T(u, t)|$  for sufficiently long time windows  $T = 1, 2.5, 5, 10, 20, 40$ . The diffusion of the orbit is nonzero, i. e. the flow is nonregular, when  $\delta F_T(u, t) > \epsilon_f$ . For the analysis of the flows presented in this study we evaluate  $F_T(u, t)$  at the time instants  $t_i = 0.1(i-1) \leq T_f - T$  and  $\delta F_T(u, t)$  at the same time instants but for  $t_i \leq T_f - 2T$ .

#### 4. Results: Analysis of chaotic flows

Several flow realisations that correspond to two different routes to chaos [45] are studied in this section. The first scenario is in accordance with the Newhouse-Ruelle-Takens route [40] in which strange attractors develop from a sequence of Hopf bifurcations giving rise to quasiperiodic flows. The second scenario corresponds to the Feigenbaum route [46] in which chaotic flows are developed after a sequence of period doubling bifurcations. These two routes have been recently identified in the MSC problem [19] in a parameter regime corresponding to the radial jet instability, in which the magnetic ef-

fects are weak. In the following, the specific problem parameters are  $\chi = 0.5$ ,  $\text{Re} = 10^3$  and  $\text{Ha} < 4$ .

We are interested in the description of long term behaviour of solutions belonging to the two scenarios as they give rise to the chaotic flows presented in [19]. We select three different flows at each of the routes (Newhouse-Ruelle-Takens and Feigenbaum) and perform the analysis summarised in Sec. 3.2 to estimate diffusion of the corresponding orbits. The flows are obtained by means of direct numerical simulations as described in [19]. The spatial resolution requirements,  $N_r = 40$  and  $L_{\max} = 84$ , for obtaining radial jet flows have been validated in [5] and, as commented in Sec. 3.1, high order time integration is employed to obtain accurate time series.

One quasiperiodic flow with three fundamental frequencies at  $\text{Ha} = 0.7$ , and two chaotic flows at  $\text{Ha} = 0.67$  and  $\text{Ha} = 0.63$  are considered for the Newhouse-Ruelle-Takens scenario. They belong to the same branch described in [19] with  $m = 1$  azimuthal symmetry and  $m_{\max} = 2$ . For the Feigenbaum route a quasiperiodic flow with two fundamental frequencies at  $\text{Ha} = 3.425$  and two chaotic flows at  $\text{Ha} = 3.4$  and  $\text{Ha} = 0.7$  are analysed. The regular and chaotic flows at  $\text{Ha} = 3.425$  and  $\text{Ha} = 3.4$  have  $m = 2$  azimuthal symmetry whereas the azimuthal symmetry of the chaotic flow at  $\text{Ha} = 0.7$  is  $m = 1$ . The latter chaotic flow, with  $m_{\max} = 2$  is more developed and originated from the period doubling cascade (flows at  $\text{Ha} = 3.425$  and  $\text{Ha} = 3.4$ ).

Figure 2 displays the time series of the radial velocity  $v_r$  and the volume averaged kinetic energy of the  $m = 2$  component of the flow  $K_2$  (see Sec. 2.3) for the regular and chaotic flows at  $\text{Ha} = 3.425$  and  $\text{Ha} = 0.7$ , respectively,

in case of the Feigenbaum scenario. For the 2-frequency solution (panels (a) and (b)), the time series of  $v_r$  exhibits a quasiperiodic behaviour whereas the time series of  $K_2$  remains periodic, showing the period-doublings. This is because the solution is a modulated rotating wave [21, 18] and one of the frequencies is associated with the rigid rotation (azimuthal drift) of the flow patterns. By azimuthally averaging the flow, only the frequency of modulation is observed. The time series of the chaotic flow at  $\text{Ha} = 0.7$

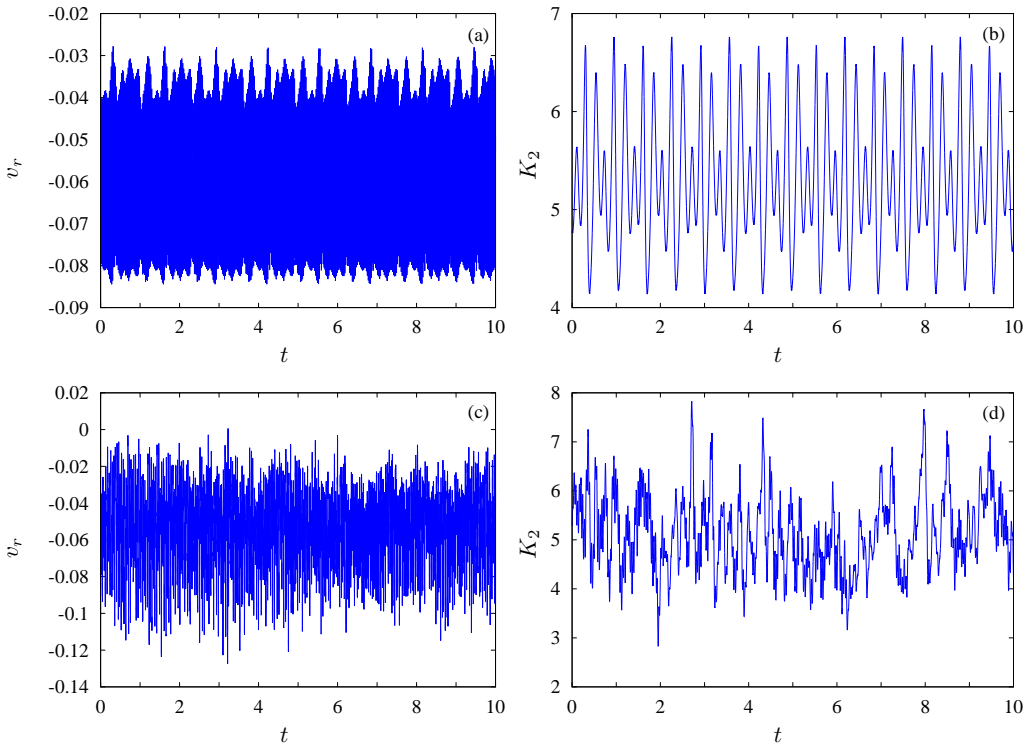


Figure 2: (a,c) The time series of the radial velocity picked up at the point  $(r, \theta, \varphi) = (r_i + 0.5d, \pi/8, 0)$ . (b,d) The time series of the volume averaged kinetic energy of the  $m = 2$  component of the flow. (a,b) Are for a regular flow with two fundamental frequencies at  $\text{Ha} = 3.425$ , and (c,d) are for a chaotic flow at  $\text{Ha} = 0.7$ .

(panels (c) and (d)) exhibit a clear chaotic behaviour, but the small temporal scale (associated to the azimuthal drift shown in panel (a)) of the radial velocity still prevails.

To visualise the typical flow topology of flows associated to the radial jet instability the contour plots for the radial velocity  $v_r$  as well as those for the kinetic energy  $\mathbf{v}^2$ , for the chaotic solution of the Feigenbaum scenario at  $\text{Ha} = 0.7$ , are shown in figure 3. For  $v_r$  the nonaxisymmetric (only  $m \neq 0$  in Eqs.5-6) as well as the total components (all  $m$ 's in Eqs.5-6) of the flow are shown. The position of the sections corresponds to the place where the nonaxisymmetric component has a relative maximum. The flow mainly consists of a radial axisymmetric jet at equatorial latitudes (see total flow sections) which is perturbed by an almost  $m = 2$  equatorially antisymmetric mode. It should be mentioned that a noticeable negative polar vortex is located near the outer surface. In agreement with this picture the kinetic energy topology behaves similarly. In this case only the component with  $m = 2$  as well as the total component of the flow are considered and the position of the sections corresponds to a local maximum of the  $m = 2$  component. Fluid motion is concentrated in the region of the radial jet but the motions are extended up to high latitudes due to the meridional circulation of the flow.

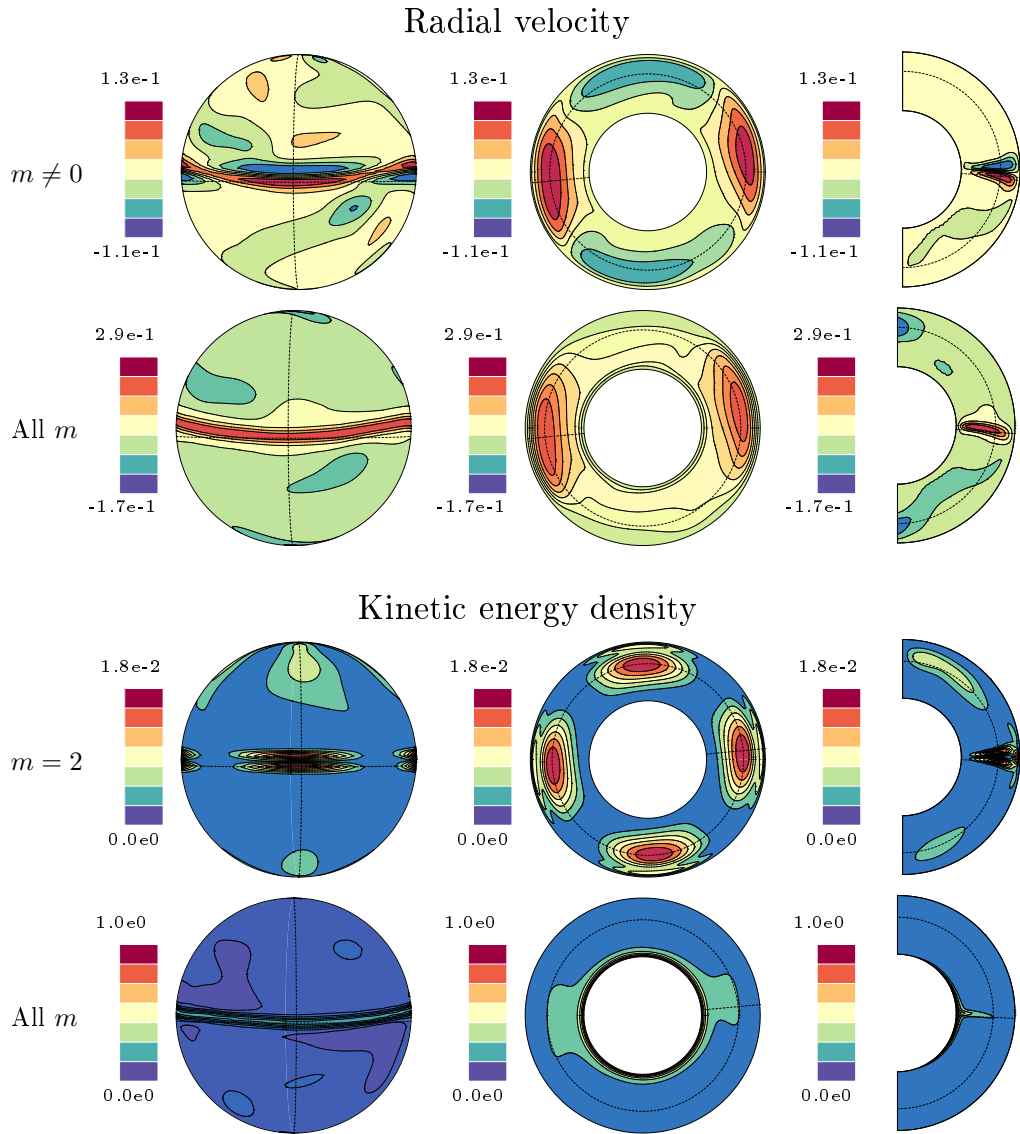


Figure 3: Contour plots for the chaotic flow at  $Ha = 0.7$ . 1st/2nd rows: nonaxisymmetric and total components of the radial velocity. 3rd/4th rows:  $m = 2$  and total components of the kinetic energy. Spherical, colatitudinal, and meridional sections are displayed on each row. For the nonaxisymmetric and the  $m = 2$  components the sections pass throughout the relative maxima of the respective field (see the dashed lines). The same position is selected for the sections of the total component for an easy comparison between both components.

#### 4.1. Newhouse-Ruelle-Takens scenario

In this section the appearance of chaos, successively at  $\text{Ha} = 0.67$  and  $\text{Ha} = 0.63$ , from a 3 frequency regular flow at  $\text{Ha} = 0.7$  is demonstrated evaluating the time evolution of the main frequency  $f$ , i. e. that with maximum amplitude (see Sec. 3.2) of two different measurables, namely, the radial velocity and the  $m = 2$  volume-averaged kinetic energy (defined in Sec.2.3). In addition, the diffusion of the different orbits in the phase space is estimated.

Figure 4(a) provides  $f(t)$  computed using a time window of  $T = 5, 10, 20, 40$  (the larger the oscillations the smaller the time window) for the regular wave with 3 fundamental frequencies at  $\text{Ha} = 0.7$ . As  $f$  is computed from the time series of  $v_r$  it corresponds to the frequency of the azimuthal drift of the wave. A very weak time dependence is observed which damps out by increasing  $T$ . For  $T \geq 10$  the relative oscillations of  $f$  are less than  $10^{-5}$  and the time difference  $\delta f(t) = |f(t+T) - f(t)| \lesssim 10^{-4}$  (see Fig. 4(b)). We assume this values to be valid for classifying this flow as regular, considering then an accuracy  $\epsilon_f = 10^{-4}$  for the frequency determination. We note that although a value of  $\epsilon_f = 10^{-5}$  was achieved in Sec. 3.1 in the case of a rotating wave (i. e. a periodic orbit), the regular solution now has 3 fundamental frequencies which may increase the uncertainty in frequency determination. For the chaotic flows at  $\text{Ha} = 0.67$  (Figs. 4(c,d)) and  $\text{Ha} = 0.63$  (Figs. 4(e,f)) the variation of  $f$  and the value of  $\delta f$  is significant and the amplitude of their oscillations is growing with time. For the chaotic flows the value of  $\delta f$  is at least one order of magnitude larger than for the regular flow, although it is still small indicating slow diffusion of the orbit in the phase space. Indeed, the range of variation of  $f$  is narrow which indicates the robustness of the

azimuthal drift in the temporal description of these flows.

The frequency description considering the  $m = 2$  volume-averaged kinetic energy, which is summarised in Fig. 5, is even more clear than that corresponding to the radial velocity. The accuracy of frequency determination improves giving rise to  $\delta f < 10^{-5}$  for time windows  $T \geq 20$  in the case of the regular flow at  $\text{Ha} = 0.7$ . This is not surprising as volume-averaging goes along with the removal of the azimuthal drift time scale from the flow so that only two fundamental frequencies are involved in the time series. In addition, for the chaotic flows at  $\text{Ha} = 0.67$  and  $\text{Ha} = 0.63$  the value of  $\delta f$  and the interval of variation of  $f$  increase by one order of magnitude with respect to the analysis of the radial velocity. As a consequence different diffusion rates of the orbit emerge within the phase space so that volume-averaging provides a better description of these chaotic flows.

To highlight the superiority of Laskar's algorithm with respect the common FFT the moving FFT frequency spectrum of the volume-averaged kinetic energy of the  $m = 2$  component of the flow is presented in Fig. 6(a,b). The top plot corresponds to a regular flow at  $\text{Ha} = 0.74$ , i. e. at a Hartmann number larger than the regular flow at  $\text{Ha} = 0.7$  presented in this section, whereas the bottom plot corresponds to the chaotic flow at  $\text{Ha} = 0.63$  with larger variation of  $f$  in Fig. 5. Although for the chaotic flow the moving spectra exhibit some irregular bands around secondary frequencies, the frequency of largest amplitude remains constant to  $f = 8.9$  at  $\text{Ha} = 0.63$  (also  $\text{Ha} = 0.67$ ), which is the same value obtained for the regular flow, at significantly different  $\text{Ha} = 0.74$ . For the figure a time window of  $T = 10$  is used, however, for large values, the results remain basically unchanged.

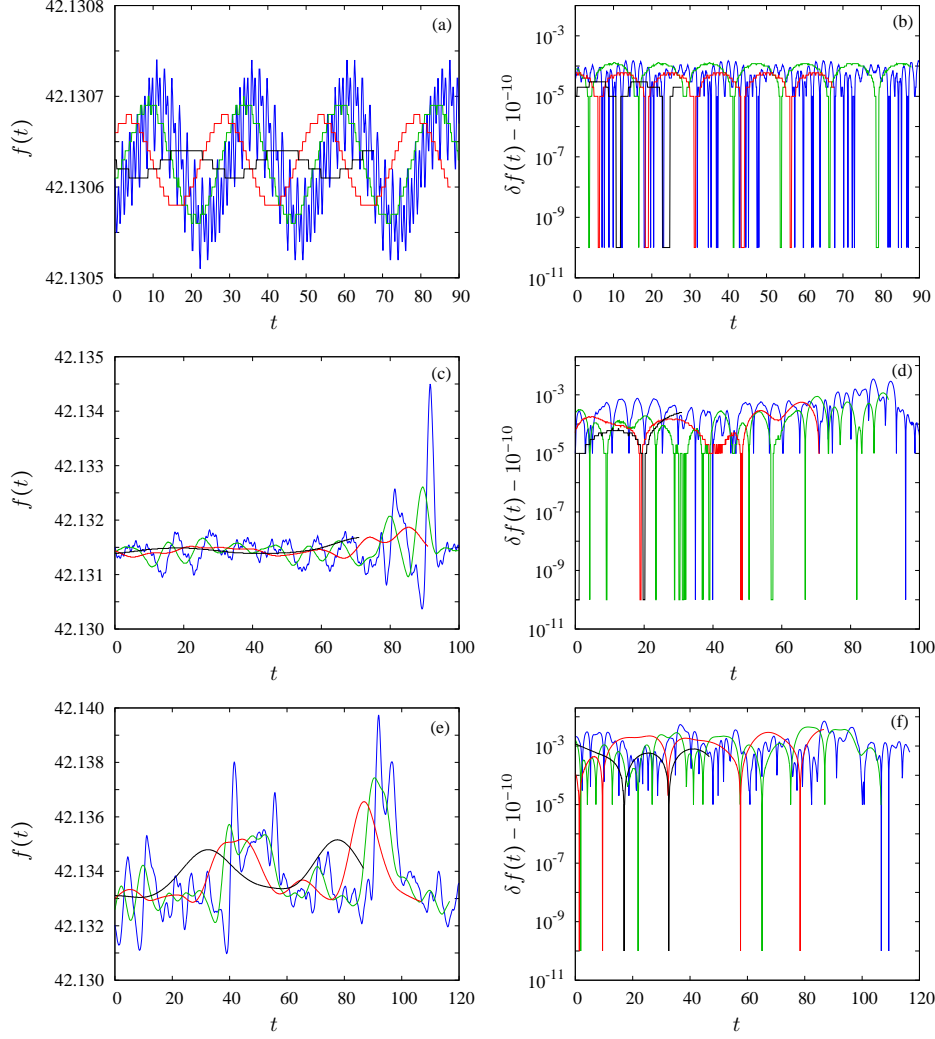


Figure 4: Time dependent frequency spectrum based on Laskar algorithm (SDDSToolKit). The time series correspond to the radial velocity picked up at the point  $(r, \theta, \varphi) = (r_i + 0.5d, \pi/8, 0)$ . (a,c,e) Frequency with maximum amplitude versus time. (b,d,f) Time difference  $\delta f(t) = |f(t+T) - f(t)|$  versus time (logscale). Different colors denote different length of the time series (blue  $T = 5$ , green  $T = 10$ , red  $T = 20$  and black  $T = 40$ ). Panels (a,b) are for a regular solution at  $\text{Ha} = 0.7$ , panels (c,d) are for a chaotic solution at  $\text{Ha} = 0.67$ , and panels (e,f) are for a chaotic solution at  $\text{Ha} = 0.63$ .

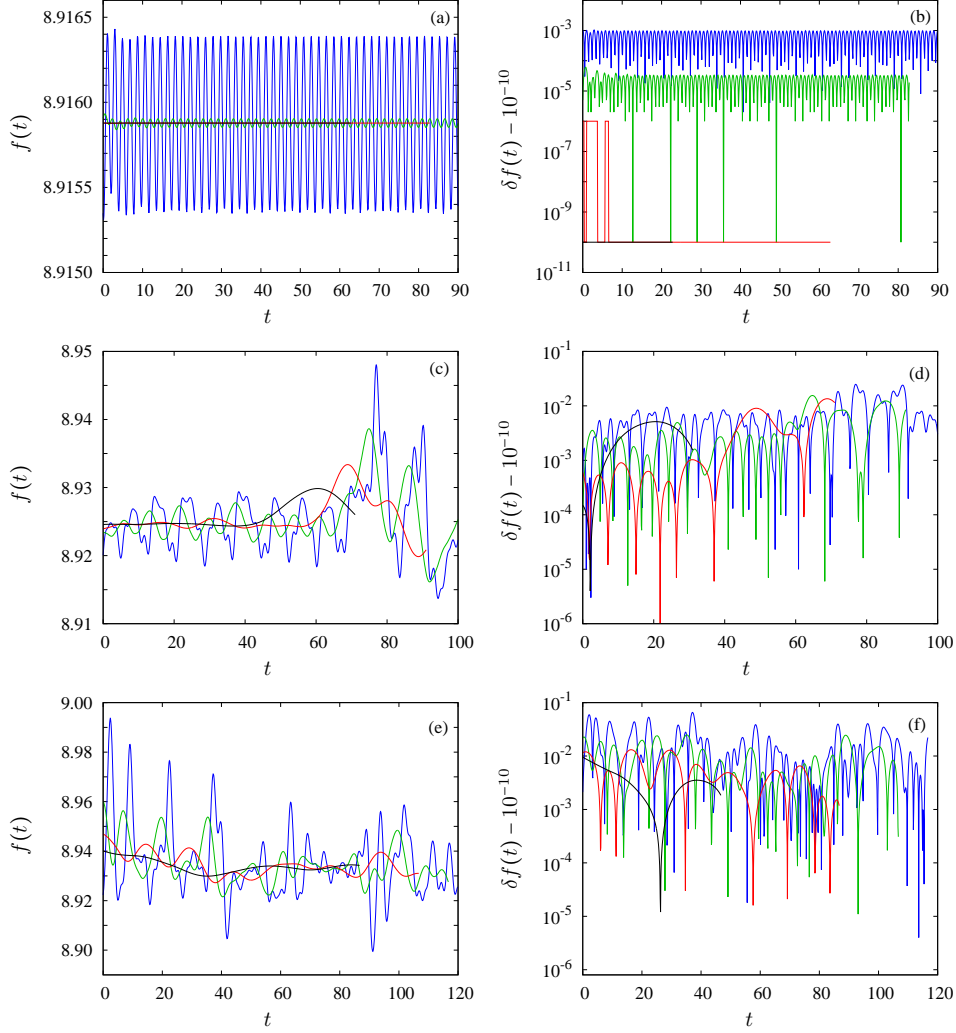


Figure 5: Time dependent frequency spectrum based on Laskar algorithm (SDDSToolKit). The time series correspond to the volume averaged kinetic energy of the  $m = 2$  component of the flow. (a,c,e) Frequency  $f$  with maximum amplitude versus time. (b,d,f) Time difference  $\delta f(t) = |f(t+T) - f(t)|$  versus time (logscale). Different colors denote different length of the time series (blue  $T = 5$ , green  $T = 10$ , red  $T = 20$  and black  $T = 40$ ). Panels (a,b) are for a regular solution at  $\text{Ha} = 0.7$ , panels (c,d) are for a chaotic solution at  $\text{Ha} = 0.67$ , and panels (e,f) are for a chaotic solution at  $\text{Ha} = 0.63$ .

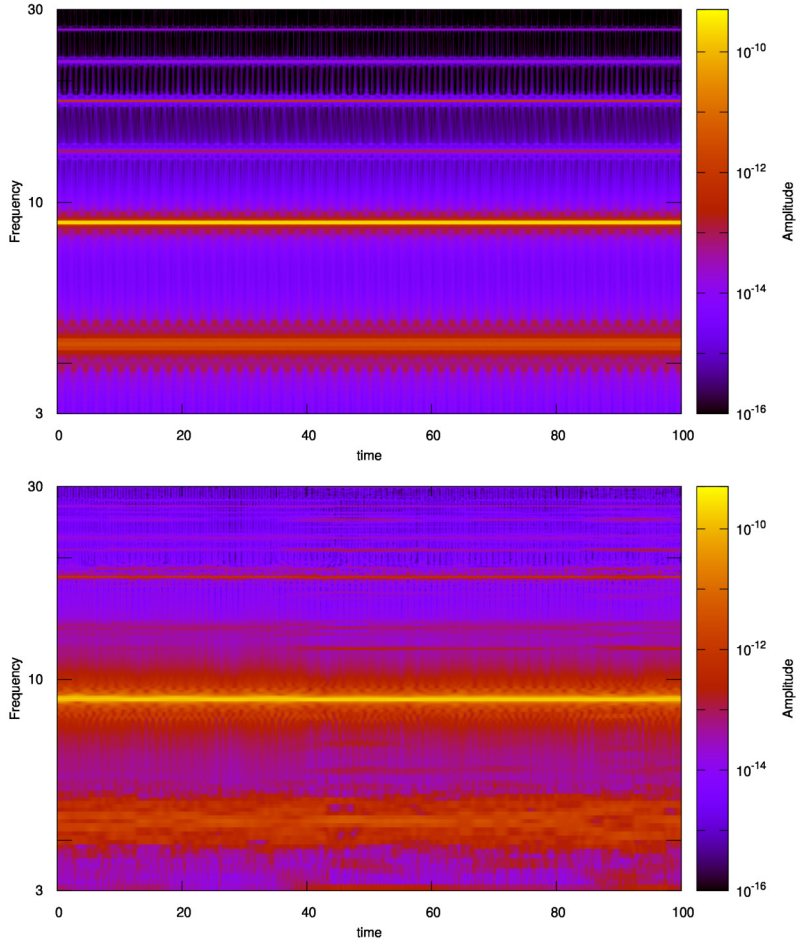


Figure 6: Time dependent frequency spectrum based on FFT on a time window  $T = 10$ . The time series correspond to the volume averaged kinetic energy of the  $m = 2$  component of the flow. (a) Three frequency quasiperiodic flow at  $Ha = 0.74$  and (b) Chaotic flow at  $Ha = 0.63$ . The frequency with maximum amplitude remains constant in the whole time range and is  $f = 8.9$ , for both  $Ha = 0.74$  and  $Ha = 0.63$ , and thus it does neither reveal the chaotic behavior for  $Ha = 0.63$  nor it reflects the dependence of  $f$  on  $Ha$ .

#### 4.2. Feigenbaum scenario

This section focuses on chaotic flows originating from a period-doubling cascade of flows with  $m = 2$  azimuthal symmetry (see [19]). The regular character of a solution at  $\text{Ha} = 3.425$  is lost after period-doublings at  $\text{Ha} = 3.4$ . As studied in [19], the chaotic nature of the flow remains by decreasing  $\text{Ha}$  giving rise to strongly oscillatory chaotic flows with azimuthal symmetry  $m = 1$  and  $m_{\text{max}} = 2$  even close to  $\text{Ha} = 0$ . A chaotic flow of this type is selected as well at  $\text{Ha} = 0.7$ .

Figure 7(a,b) illustrates the analysis of the radial velocity time series of the regular solution at  $\text{Ha} = 3.425$ , corresponding to a quasiperiodic flow with two fundamental frequencies (a modulated rotating wave [18]) and with azimuthal symmetry  $m = 2$ . In comparison with the regular solution of the Newhouse-Ruelle-Takens scenario, the variation of the frequency with maximum amplitude  $f$  and the value of  $\delta f$  is clearly smaller for a fixed time window  $T$ . Indeed, for  $T \geq 20$  the value of  $f$  is constant within  $\epsilon_f = 10^{-7}$ . Furthermore, the regular solution for the Feigenbaum scenario has two fundamental frequencies whereas that of the Newhouse-Ruelle-Takens scenario has three, which may be the reason for the smaller value of  $\epsilon_f$  achieved for the regular solution in case of the Feigenbaum route.

Because the flow at  $\text{Ha} = 3.4$  is close to the origin of period-doubling chaos, the range of variation of  $f$  and  $\delta f$  is small but relevant, providing a chaotic signature (see Fig. 7(c,d)). For the largest time window considered  $T = 40$  the difference value is  $\delta t \leq 10^{-5}$ , clearly larger than  $\epsilon_f = 10^{-7}$ . The values for  $f$  and  $\delta f$  for the chaotic flow at  $\text{Ha} = 0.7$  (shown in Fig. 7(e,f)) are more pronounced but still remain small. For instance,  $f$  oscillates around

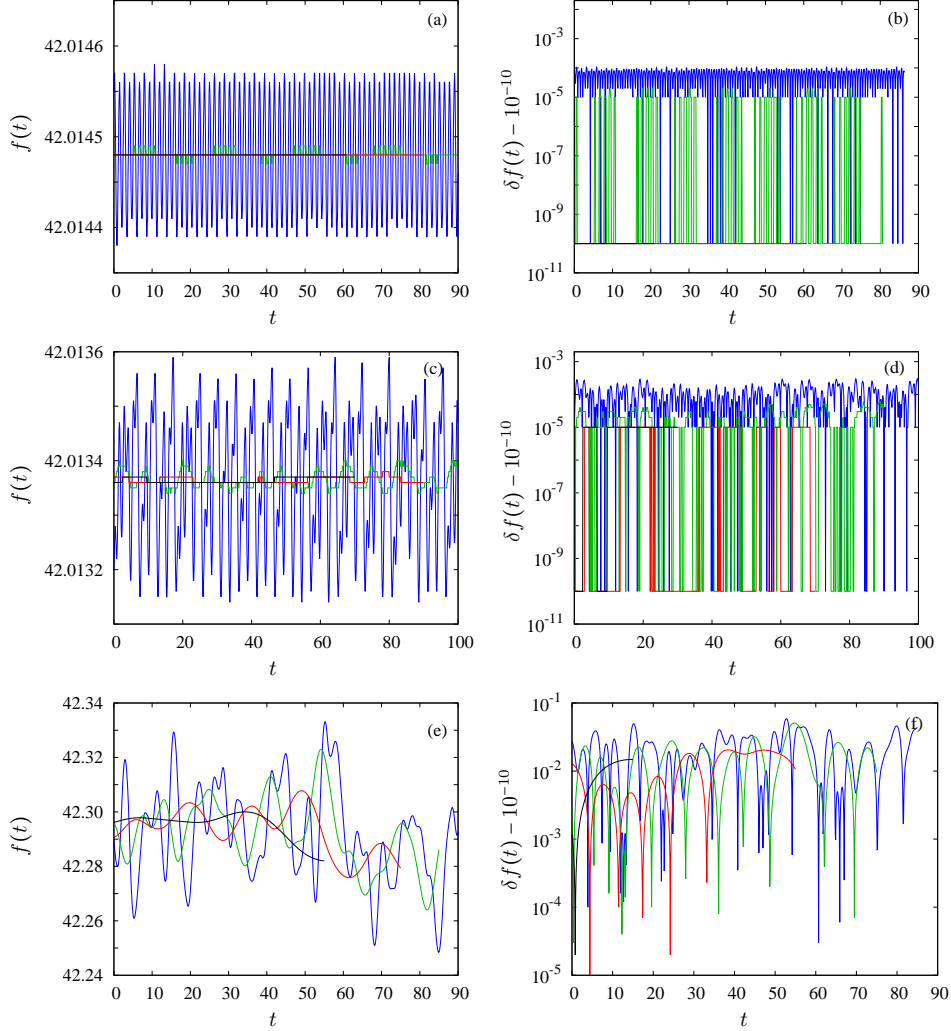


Figure 7: Time dependent frequency spectrum based on Laskar algorithm (SDDSToolKit). The time series correspond to the radial velocity picked up at the point  $(r, \theta, \varphi) = (r_i + 0.5d, \pi/8, 0)$ . (a,c) Frequency with maximum amplitude versus time. (b,d) Time difference  $\delta f(t) = |f(t+T) - f(t)|$  versus time (logscale). Different colours denote different lengths of the time series (blue  $T = 5$ , green  $T = 10$ , red  $T = 20$  and black  $T = 40$ ). Panels (a,b) are for a regular solution at  $\text{Ha} = 3.425$ , panels (c,d) are for a chaotic solution at  $\text{Ha} = 3.4$ , and panels (e,f) for a chaotic solution at  $\text{Ha} = 0.7$ .

its mean value with less than 1% for all considered time windows  $T$ , which indicates the robust character of the frequency associated to the azimuthal drift, even for this highly oscillatory flow.

As for the Newhouse-Ruelle-Takens scenario the analysis for the volume averaged kinetic energy of the  $m = 2$  component of the flow, summarised in Fig. 8, provides a better measure of chaotic behaviour. We note that for the regular solution a slightly noticeable transient can be identified on Fig. 8(a,b), because of the regular solution at  $Ha = 3.425$  being close to the second period doubling bifurcation at  $Ha_2 = 3.423$  (see [19] for details), so that long transients can be expected. Nevertheless values of  $\delta f < 10^{-5}$ , for  $T \geq 20$ , are obtained, which supports our assumption of  $\epsilon_f = 10^{-5}$  for the largest time windows. The value of  $\delta f$  is clearly larger than this threshold (for  $T \geq 20$ ) when analysing the chaotic solution at  $Ha = 3.4$  (see Fig. 8(d)).

In contrast to the previous chaotic flows, the description for the highly oscillatory flow at  $Ha = 0.7$  is substantially different (see Fig. 8(e,f)). In this case, the frequency  $f$  spans around two orders of magnitude and the values of  $\delta f$  raise up to  $O(10)$ , accounting for a wide range of temporal scales in volume-averaged quantities. We recall that this was not the case for the main frequency of the radial velocity displayed in Fig. 7(e,f). To highlight the differences between the main time scales of the flow and those of volume-averaged quantities the time dependent spectrum based on FFT is provided in Fig. 9. With the FFT analysis and a time window of  $T = 10$  the frequency of maximum amplitude of the flow remains constant at  $f = 42.3$  whereas a broad band of main frequencies is obtained in case of the volume-averaged kinetic energy of the  $m = 2$  component of the flow.

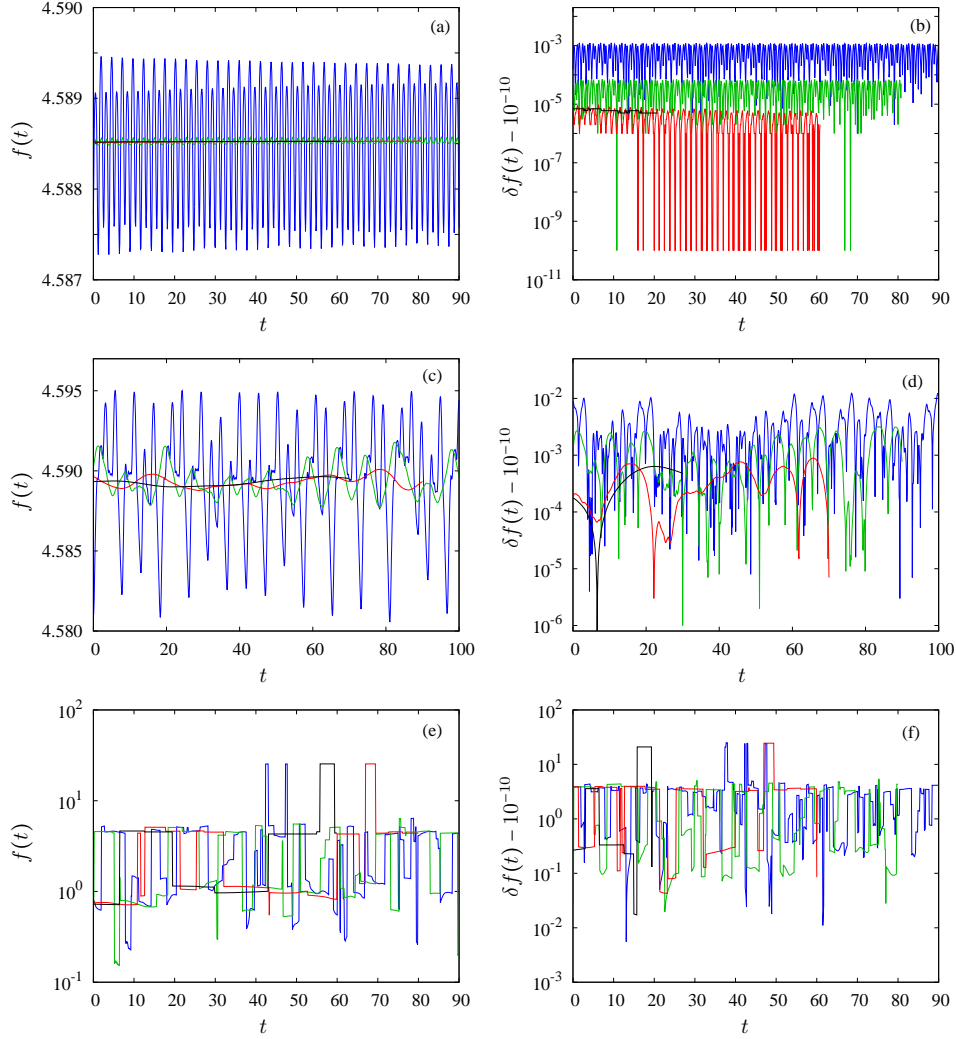


Figure 8: Time dependent frequency spectrum based on Laskar algorithm (SDDSToolKit). The time series corresponds to the volume averaged kinetic energy of the  $m = 2$  component of the flow. (a,c) Frequency with maximum amplitude versus time. (b,d) Time difference  $\delta f(t) = |f(t+T) - f(t)|$  versus time (logscale). Different colors denote different lengths of the time series (blue  $T = 5$ , green  $T = 10$ , red  $T = 20$  and black  $T = 40$ ). Panels (a,b) are for a regular solution at  $Ha = 3.425$ , panels (c,d) are for a chaotic solution at  $Ha = 3.4$ , and panels (e,f) for a chaotic solution at  $Ha = 0.7$ .

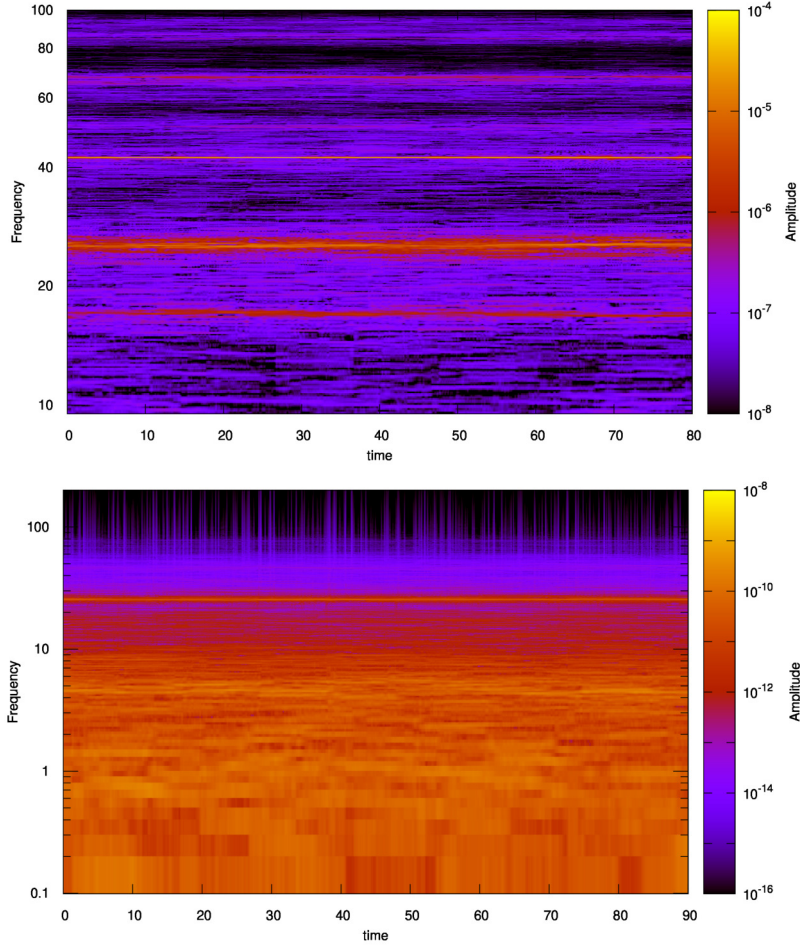


Figure 9: Time dependent frequency spectrum based on FFT on a time window  $T = 10$  for the chaotic flow at  $\text{Ha} = 0.7$ . The time series correspond to (a) the radial velocity picked up at the point  $(r, \theta, \varphi) = (r_i + 0.5d, \pi/8, 0)$  and (b) the volume averaged kinetic energy of the  $m = 2$  component of the flow. For the volume-averaged kinetic energy, the frequency with maximum amplitude varies on a broad range  $f \in (0.1, 100)$ . In contrast, for the time series corresponding to the local measurement (radial velocity) the frequency with maximum amplitude remains constant ( $f = 42.3$ ) in the whole time range.

## 5. Summary and conclusions

The present study is based on very long time high order time integrations of the MSC equations, with a discretized system of  $O(10^5)$  degrees of freedom. Specifically the DNS, on a spherical shell with an aspect ratio  $\chi = 0.5$ , cover 100 viscous time units at a Reynolds number  $\text{Re} = 10^3$ . This represents around  $1.6 \times 10^4$  inner sphere rotation periods, which is a value two orders of magnitude larger than the achieved by previous studies in the field [2, 4]. In S.I. units the DNS span about 7 days, which is clearly large when compared with a typical run ( $\sim 8\text{h}$ ) of the HEDGEHOG experiment [16].

The time series of local (the radial velocity at a point inside the shell) and global (a volume-averaged kinetic energy) measurables have been analysed using Laskar's algorithm for the determination of fundamental frequencies [26]. The accuracy of the method (down to  $10^{-7}$  in relative values) is estimated using a periodic flow (a rotating wave) from which the frequency can be obtained using a Newton-Krylov procedure [5].

Several regular and chaotic flows found in [19] are selected for the analysis. First, one regular and two chaotic flows representing the Newhouse-Ruelle-Takens scenario [40] are investigated. Similarly, one regular and two chaotic flows from the Feigenbaum scenario [46] are selected as well. Following [28], the frequency of maximum amplitude  $f$  is computed on several time windows  $T \leq 40$  to study the time dependence of  $f(t)$  and  $\delta f = |F(t+T) - f(t)|$ . This reveals the existence of chaos and helps to estimate the diffusion of the orbit in the phase space.

Table 1: Mean frequency  $\bar{f}$  with maximum amplitude, and its absolute difference  $\varepsilon_f = f_{\max} - f_{\min}$ . The time dependent frequency of maximum amplitude  $f$  is computed on a time window  $T$  from the time series of the radial velocity picked up at the point  $(r, \theta, \varphi) = (r_i + 0.5d, \pi/8, 0)$ . This frequency is associated to the drifting behaviour of the waves.

		Newhouse-Ruelle-Takens			Feigenbaum		
$T$	Ha	0.7*	0.67	0.63	3.425*	3.4	0.7
1	$\bar{f}$	42.13	42.13	42.13	42.01	42.01	40
1	$\varepsilon_f$	$3 \times 10^{-2}$	$4 \times 10^{-2}$	$6 \times 10^{-2}$	$4 \times 10^{-2}$	$5 \times 10^{-2}$	20
2.5	$\bar{f}$	42.131	42.13	42.13	42.014	42.013	42
2.5	$\varepsilon_f$	$4 \times 10^{-3}$	$10^{-2}$	$2 \times 10^{-2}$	$4 \times 10^{-3}$	$6 \times 10^{-3}$	17
5	$\bar{f}$	42.1303	42.132	42.134	42.0144	42.0131	42.29
5	$\varepsilon_f$	$2 \times 10^{-4}$	$4 \times 10^{-3}$	$9 \times 10^{-3}$	$2 \times 10^{-4}$	$5 \times 10^{-4}$	$8 \times 10^{-2}$
10	$\bar{f}$	42.1304	42.132	42.134	42.01448	42.01337	42.29
10	$\varepsilon_f$	$10^{-4}$	$2 \times 10^{-3}$	$5 \times 10^{-3}$	$2 \times 10^{-5}$	$6 \times 10^{-5}$	$6 \times 10^{-2}$
20	$\bar{f}$	42.13057	42.1316	42.134	42.014481	42.01337	42.29
20	$\varepsilon_f$	$9 \times 10^{-5}$	$6 \times 10^{-4}$	$4 \times 10^{-3}$	0	$2 \times 10^{-5}$	$3 \times 10^{-2}$
40	$\bar{f}$	42.13082	42.1313	42.134	42.014481	42.01336	42.295
40	$\varepsilon_f$	$3 \times 10^{-5}$	$3 \times 10^{-4}$	$2 \times 10^{-3}$	0	$10^{-5}$	$2 \times 10^{-2}$

Table 2: Mean frequency  $\bar{f}$  with maximum amplitude, and its absolute difference  $\varepsilon_f = f_{\max} - f_{\min}$ . The time dependent frequency of maximum amplitude  $f$  is computed on a time window  $T$  from the time series of the volume averaged kinetic energy of the  $m = 2$  component of the flow. This frequency is associated to the modulation behaviour of the waves.

		Newhouse-Ruelle-Takens			Feigenbaum		
$T$	Ha	0.7*	0.67	0.63	3.425*	3.4	0.7
1	$\bar{f}$	8.92	8.9	8.9	4.5	4.5	4
1	$\varepsilon_f$	$7 \times 10^{-2}$	$2 \times 10^{-1}$	$2 \times 10^{-1}$	$10^0$	$10^0$	25
2.5	$\bar{f}$	8.92	8.93	8.9	4.59	4.59	25
2.5	$\varepsilon_f$	$3 \times 10^{-2}$	$8 \times 10^{-2}$	$10^{-1}$	$5 \times 10^{-2}$	$8 \times 10^{-2}$	3
5	$\bar{f}$	8.916	8.93	8.94	4.589	4.59	25
5	$\varepsilon_f$	$10^{-3}$	$3 \times 10^{-2}$	$9 \times 10^{-2}$	$2 \times 10^{-3}$	$10^{-2}$	3
10	$\bar{f}$	8.91589	8.93	8.93	4.58856	4.589	6
10	$\varepsilon_f$	$9 \times 10^{-5}$	$2 \times 10^{-2}$	$4 \times 10^{-2}$	$9 \times 10^{-5}$	$4 \times 10^{-3}$	3
20	$\bar{f}$	8.915878	8.93	8.93	4.58852	4.589	25
20	$\varepsilon_f$	$2 \times 10^{-6}$	$10^{-2}$	$2 \times 10^{-2}$	$2 \times 10^{-5}$	$10^{-3}$	3
40	$\bar{f}$	8.9158783	8.926	8.93	4.588518	4.5893	25
40	$\varepsilon_f$	0	$6 \times 10^{-3}$	$10^{-2}$	$2 \times 10^{-6}$	$6 \times 10^{-4}$	4

The results are summarised in Tables 1 and 2 and in figure 10. From the tables as well as from the figure it can be concluded that a minimum time window of  $T = 5$  viscous time units should be used to obtain reliable results that allow an identification of chaos. In case of a local measure (the radial velocity) the range of variation of the frequency  $\varepsilon_f = f_{\max} - f_{\min}$  is significantly smaller (Table 1) than the range of variation  $\varepsilon_f$  when the global

measure (volume-averaged) is considered (Table 2). This is also true when considering the relative difference  $\max_t(\delta f)/\bar{f}$  displayed in Fig. 10. The latter evidences different diffusion rates in the phase space as the measured frequencies are obtained from different components (total or volume-averaged) of the flow.

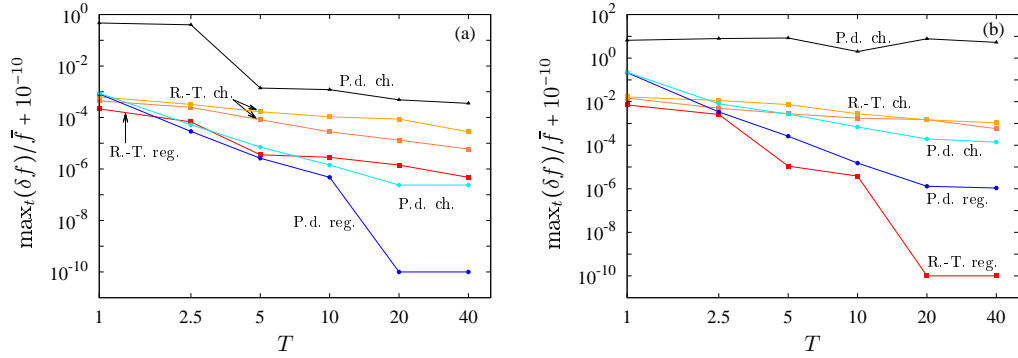


Figure 10: Relative difference  $\max_t(\delta f)/\bar{f}$ , with  $\delta f(t) = |f(t+T) - f(t)|$  and  $t \in [0, 100]$ , versus the time interval  $T$  for the Newhouse-Ruelle-Takens (R.-T., full squares), Feigenbaum (P.d., full circles and triangle) scenarios. Regular (reg.) flows for the R.-T. and P.d. scenarios are considered as well. The time series correspond to (a) the volume averaged kinetic energy of the  $m = 2$  component of the flow and (b) the radial velocity picked up at the point  $(r, \theta, \varphi) = (r_i + 0.5d, \pi/8, 0)$ .

A remarkable result is that for all types of flows, the frequency corresponding to the mean azimuthal drift (measured from the radial velocity) remains nearly constant and only oscillates less than 0.2% with respect to its mean value giving rise to very small ( $< 10^{-2}$ ) diffusion rates. This is especially surprising in the case of the highly oscillatory chaotic flow from the Feigenbaum scenario at  $Ha = 0.7$ , as the frequency corresponding to the main time scale of a volume-averaged quantity can vary more than one order

of magnitude. We have tested other chaotic flows in the same branch with  $\text{Ha} \in [0, 1.2]$  (from [19]) and the results are similar. We note that we have considered all classes of chaotic flows found in [19]. The main conclusion is then that the azimuthal drift behaviour of flows at moderate Reynolds number  $\text{Re} = 10^3$  is strongly robust, even for highly oscillatory chaotic flows and thus in this regime represents a well suited quantity to be measured in any experiment.

As found in [19], for each class of flows with azimuthal mode  $m_{\text{max}}$ , mostly contributing to the kinetic energy, the frequency associated with the azimuthal drift was very close to that of the unstable rotating wave with azimuthal symmetry  $m_{\text{max}}$ , at the same Hartmann number. With the present analysis we have demonstrated that this frequency is indeed quite robust even when considering long time integrations. Thus, unstable rotating waves provide a good description of the main time scale of the MSC flow at moderate  $\text{Re} = 10^3$  and  $\text{Ha} < 6$ .

## Acknowledgments

F. Garcia kindly acknowledges the Alexander von Humboldt Foundation for its financial support. This project has also received funding from the European Research Council (ERC) under the European Unions Horizon 2020 research and innovation programme (grant agreement No 787544).

## References

- [1] R. Hollerbach, S. Skinner, Instabilities of magnetically induced shear layers and jets, *Proc. Roy. Soc. Lond. A* 457 (2001) 785–802.
- [2] R. Hollerbach, Non-axisymmetric instabilities in magnetic spherical Couette flow, *Proc. Roy. Soc. Lond. A* 465 (2009) 2003–2013.
- [3] C. Gissinger, H. Ji, J. Goodman, Instabilities in magnetized spherical Couette flow, *Phys. Rev. E* 84 (2011) 026308.
- [4] E. J. Kaplan, Saturation of nonaxisymmetric instabilities of magnetized spherical Couette flow, *Phys. Rev. E* 89 (063016) (2014) 1–8.
- [5] F. Garcia, F. Stefani, Continuation and stability of rotating waves in the magnetized spherical Couette system: Secondary transitions and multistability, *Proc. Roy. Soc. Lond. A* 474 (2018) 20180281.
- [6] E. Dormy, A. M. Soward (Eds.), *Mathematical Aspects of Natural Dynamos*, Vol. 13 of *The Fluid Mechanics of Astrophysics and Geophysics*, Chapman & Hall/CRC, Boca Raton, FL, 2007.
- [7] K. Moffat, E. Dormy, *Self-Exciting Fluid Dynamos*, *Cambridge Texts in Applied Mathematics*, Cambridge University press, 2019.
- [8] G. Rüdiger, *Differential Rotation and Stellar Convection: Sun and Solar-type Stars*, *Fluid mechanics of astrophysics and geophysics*, Gordon and Breach Science Publishers, 1989.
- [9] C. A. Jones, Planetary magnetic fields and fluid dynamos, *Ann. Rev. Fluid Mech.* 43 (1) (2011) 583–614.

- [10] H. Ji, S. Balbus, Angular momentum transport in astrophysics and in the lab, *Phys. Today* 66 (8) (2013) 27–33.
- [11] S. A. Balbus, J. F. Hawley, A powerful local shear instability in weakly magnetized disks. i- Linear analysis. ii- Nonlinear evolution, *Astrophys. J.* 376 (1991) 214–233.
- [12] F. Stefani, T. Gundrum, G. Gerbeth, G. Rüdiger, M. Schultz, J. Szklarski, R. Hollerbach, Experimental evidence for magnetorotational instability in a Taylor-Couette flow under the influence of a helical magnetic field, *Phys. Rev. Lett.* 97 (2006) 184502.
- [13] F. Stefani, G. Gerbeth, T. Gundrum, R. Hollerbach, J. Priede, G. Rüdiger, J. Szklarski, Helical magnetorotational instability in a Taylor-Couette flow with strongly reduced Ekman pumping, *Phys. Rev. E* 80 (2009) 066303.
- [14] M. Seilmayer, V. Galindo, G. Gerbeth, T. Gundrum, F. Stefani, M. Gellert, G. Rüdiger, M. Schultz, R. Hollerbach, Experimental evidence for nonaxisymmetric magnetorotational instability in a rotating liquid metal exposed to an azimuthal magnetic field, *Phys. Rev. Lett.* 113 (2014) 024505.
- [15] D. R. Sisan, N. Mujica, W. A. Tillotson, Y. M. Huang, W. Dorland, A. B. Hassam, T. M. Antonsen, D. P. Lathrop, Experimental observation and characterization of the magnetorotational instability, *Phys. Rev. Lett.* 93 (2004) 114502.

- [16] C. Kasprzyk, E. Kaplan, M. Seilmayer, F. Stefani, Transitions in a magnetized quasi-laminar spherical Couette flow, *Magnetohydrodynamics* 53 (2) (2017) 393–401.
- [17] V. Travnikov, K. Eckert, S. Odenbach, Influence of an axial magnetic field on the stability of spherical Couette flows with different gap widths, *Acta Mech.* 219 (2011) 255–268.
- [18] F. Garcia, M. Seilmayer, A. Giesecke, F. Stefani, Modulated rotating waves in the magnetized spherical Couette system, *J. Nonlinear Sci.* 29 (2019) 2735–2759.
- [19] F. Garcia, M. Seilmayer, A. Giesecke, F. Stefani, Chaotic wave dynamics in weakly magnetised spherical Couette flows, *CHAOS* (2020).
- [20] J. D. Crawford, E. Knobloch, Symmetry and symmetry-breaking bifurcations in fluid dynamics, *Ann. Rev. Fluid Mech.* 23 (1) (1991) 341–387.
- [21] D. Rand, Dynamics and symmetry. Predictions for modulated waves in rotating fluids, *Arch. Ration. Mech. An.* 79 (1) (1982) 1–37.
- [22] M. Golubitsky, V. G. LeBlanc, I. Melbourne, Hopf bifurcation from rotating waves and patterns in physical space, *J. Nonlinear Sci.* 10 (2000) 69–101.
- [23] M. Golubitsky, I. Stewart, *The symmetry perspective: From equilibrium to chaos in phase space and physical space.*, Birkhäuser, Basel, 2003.
- [24] J. Laskar, The chaotic motion of the solar system: A numerical estimate of the size of the chaotic zones, *Icarus* 88 (2) (1990) 266 – 291.

- [25] J. Laskar, C. Froeschlé, A. Celletti, The measure of chaos by the numerical analysis of the fundamental frequencies. application to the standard mapping, *Physica D* 56 (2) (1992) 253 – 269.
- [26] J. Laskar, Frequency analysis of a dynamical system, *Celestial Mech. Dyn. Astr.* 56 (1993) 191–196.
- [27] M. Borland, L. Emery, H. Shang, R. Soliday, User’s Guide for SDDS Toolkit Version 1.30, It is available on the web at <http://www.aps.anl.gov/asd/oag/software.shtml> (2005).
- [28] J. Laskar, Frequency analysis for multi-dimensional systems. Global dynamics and diffusion, *Physica D* 67 (1993) 257–281.
- [29] G. Gómez, J. M. Mondelo, C. Simó, A collocation method for the numerical fourier analysis of quasi-periodic functions. I: Numerical tests and examples, *Discrete Cont. Dyn. B* 14 (1) (2010) 41–74.
- [30] G. Gómez, J. M. Mondelo, C. Simó, A collocation method for the numerical Fourier analysis of quasi-periodic functions. II: Analytical error estimates, *Discrete Cont. Dyn. B* 14 (1) (2010) 75–109.
- [31] I. Djurović, V. Rubezić, Chaos detection in chaotic systems with large number of components in spectral domain, *Signal Processing* 88 (9) (2008) 2357–2362.
- [32] M. Varanis, J. Norenberg, R. Rocha, C. Oliveira, J. Balthazar, A. Tuset, A comparison of time-frequency methods for nonlinear dynamics and chaos analysis in an energy harvesting model, *Braz. J. Phys.* (2020).

- [33] V. I. Oseledec, A multiplicative ergodic theorem: Lyapunov characteristic numbers for dynamical systems, *Trans. Moscow Math. Soc.* 19 (1968) 197–231.
- [34] G. Benettin, L. Galgani, A. Giorgilli, J. M. Strelcyn, Lyapunov characteristic exponents for smooth dynamical systems and for Hamiltonian systems: A method for computing all of them, *Meccanica* 15 (1980) 9–20.
- [35] R. Grappin, J. Léorat, Lyapunov exponents and the dimension of periodic incompressible Navier-Stokes flows: numerical measurements, *J. Fluid Mech.* 222 (1991) 61–94.
- [36] R. Hegger, H. Kantz, T. Schreiber, Practical implementation of nonlinear time series methods: The tisean package, *CHAOS* 413 (1999).
- [37] F. Takens, Detecting strange attractors in turbulence, *Lecture Notes in Math.* 898 (1981).
- [38] J. Awrejcewicz, A. Krysko, N. Erofeev, V. Dobriyan, M. Barulina, V. Krysko, Quantifying chaos by various computational methods. Part 1: Simple systems, *Entropy* 20 (175) (2018).
- [39] J. Awrejcewicz, A. Krysko, N. Erofeev, V. Dobriyan, M. Barulina, V. Krysko, Quantifying chaos by various computational methods. Part 2: Vibrations of the Bernoulli–Euler beam subjected to periodic and colored noise, *Entropy* 20 (170) (2018).
- [40] S. Newhouse, D. Ruelle, F. Takens, Occurrence of strange axiom A

- attractors near quasiperiodic flows on  $t^m$ ,  $m \geq 3$ , Commun. Math. Phys. 64 (1978) 35–40.
- [41] Y. Plevachuk, V. Sklyarchuk, S. Eckert, G. Gerbeth, R. Novakovic, Thermophysical properties of the liquid Ga-In-Sn eutectic alloy, J. Chem. Eng. Data 59 (3) (2014) 757–763.
- [42] M. Frigo, S. G. Johnson, The design and implementation of FFTW3, Proceedings of the IEEE 93 (2) (2005) 216–231, special issue on "Program Generation, Optimization, and Platform Adaptation".
- [43] K. Goto, R. A. van de Geijn, Anatomy of high-performance matrix multiplication, ACM Trans. Math. Softw. 34 (3) (2008) 1–25.
- [44] F. Garcia, M. Net, B. García-Archilla, J. Sánchez, A comparison of high-order time integrators for thermal convection in rotating spherical shells, J. Comput. Phys. 229 (2010) 7997–8010.
- [45] J.-P. Eckmann, Roads to turbulence in dissipative dynamical systems, Rev. Modern Phys. 53 (4) (1981) 643–654.
- [46] M. J. Feigenbaum, Quantitative universality for a class of nonlinear transformations, J. Stat. Phys. 19 (1978) 25–52.